Bone Reports 9 (2018) 188–198

Contents lists available at ScienceDirect

Bone Reports

journal homepage: www.elsevier.com/locate/bonr

Cortical bone is an extraneuronal site of norepinephrine uptake in adult mice

Yuantee Zhu[a,b], Yun Ma[b], Florent Elefteriou[b,c,*]

[a] Department of Pharmacology, Vanderbilt University School of Medicine, Nashville, TN, United States
[b] Department of Orthopedics, Baylor College of Medicine, Houston, TX, United States
[c] Department of Molecular and Human Genetics, Baylor College of Medicine, Houston, TX, United States

ARTICLE INFO

Keywords:
Sympathetic nerves
Bone remodeling
Norepinephrine
Transporter
Uptake
Osteocyte
Tracing
Imaging
Aging

ABSTRACT

The sympathetic nervous system is a major efferent pathway through which the central nervous system controls the function of peripheral organs. Genetic and pharmacologic evidence in mice indicated that stimulation of the β2 adrenergic receptor (β2AR) in osteoblasts promotes bone loss, leading to the paradigm that high sympathetic nervous activity is deleterious to bone mass. However, considerably less data exist to understand the putative impact of endogenous norepinephrine (NE), released by sympathetic nerves, on bone homeostasis. In this study, we investigated the in vivo expression and activity of the norepinephrine transporter (NET), a membrane pump known to actively uptake NE from the extracellular space in presynaptic neurons. Consistent with previously published in vitro data showing NET uptake activity in differentiated osteoblasts, we were able to detect active NET-specific NE uptake in the mouse cortical bone compartment in vivo. This uptake was the highest in young mice and accordingly with an age-related reduction in NET uptake, NE bone content increased whereas *Net* RNA and protein expression decreased with age. Histologically, NET expression in adult mouse bones was detected in osteocytes via immunofluorescence. Lastly, taking advantage of tissue-specific fluorescent reporter mice, we used CLARITY imaging and light sheet microscopy to visualize the 3D distribution of sympathetic fibers in whole mount preparations of bone tissues. These analyses allowed us to detect tyrosine hydroxylase (TH)-positive sympathetic nerve fibers penetrating the cortical bone, where NET^+ osteocytes reside. Together, these in vitro results support the existence of an age-dependent extraneuronal and osteocytic function of NET with potential to buffer the bone catabolic action of endogenous NE released by sympathetic nerves in vivo.

1. Introduction

The skeleton is classically understood to be a structural organ allowing body movements, organ protection, and a site for hematopoiesis and calcium storage. However, recent advances in mouse models support a function of this organ in additional physiological processes, including energy metabolism (Rosen, 2016; Wei et al., 2015; Sato et al., 2013), behavior (Khrimian et al., 2017), reproduction (Oury et al., 2013; Karsenty and Oury, 2014), and as an endocrine organ (Fukumoto and Martin, 2009; DiGirolamo et al., 2012). As such, the skeleton can be expected to be both the target and the source of endocrine, paracrine, and neuronal signals that integrate its functions with other tissues and organs. Multiple experimental evidence in mice and humans suggest that the sympathetic nervous system (SNS), a branch of the autonomic nervous system responsible for maintaining the homeostasis of many tissues, regulates skeletal homeostasis (Yirmiya et al., 2006; Kajimura et al., 2011; Elefteriou et al., 2005). Sympathetic nerve fibers indeed were shown to innervate skeletal tissues (Yamazaki and Allen, 1990; Dénes et al., 2005; Chartier et al., 2018; Chartier et al., 2014), and osteoblasts express receptors for norepinephrine (NE), the neurotransmitter released by these sympathetic nerves, with the β2-adrenergic receptor (β2AR) being the predominant receptor expressed in this lineage (Elefteriou et al., 2005). The current model of how peripheral sympathetic nerves impact bone remodeling includes the release of NE, which acts on osteoblastic β2AR to promote bone loss through RANKL-mediated activation of osteoclasts (Kajimura et al., 2011; Elefteriou et al., 2005) and inhibition of osteoblast proliferation via *Clock* genes (Fu et al., 2005; Rosen, 2008). This model is derived from genetic mouse models as well as pharmacological approaches targeting mainly post-synaptic βARs, although mice lacking *Foxo1* in

* Corresponding author at: Departments of Molecular and Human Genetics, Department of Orthopedic Surgery at Baylor College of Medicine, Houston, TX, United States.
E-mail address: florent.elefteriou@bcm.edu (F. Elefteriou).

https://doi.org/10.1016/j.bonr.2018.11.002
Received 22 August 2018; Received in revised form 23 October 2018; Accepted 21 November 2018
Available online 24 November 2018

Dbh-positive pre-synaptic noradrenergic neurons also support the role of endogenous NE in controlling bone remodeling (Kajimura et al., 2014).

A number of observations also suggest sympathetic signaling may contribute to the continuous bone loss associated with aging. Sympathetic activity in post-menopausal women with osteoporosis was measured to be higher compared to post-menopausal women without osteoporosis (Farr et al., 2012). In these studies, sympathetic nerve activity was inversely correlated with trabecular bone volume fraction, thickness and compressive bone strength. This association is further supported by indirect observations showing that bone resorption is increased in patients with pheochromocytoma (Veldhuis-Vlug et al., 2012). Additionally, several retrospective studies showed that β-blockers had a beneficial effect on BMD and fracture risk (Yang et al., 2012; Turker et al., 2006; Graham et al., 2008; Eastell et al., 2016; Yang et al., 2011; Wiens et al., 2006; Toulis et al., 2014; Song et al., 2012; Reid et al., 2005; Rejnmark et al., 2004; Bonnet et al., 2007). In mice, deletion of SNS-related genes *Dbh* (Takeda et al., 2002), *Foxo1* (Rached et al., 2010), or *Adrb2* (Elefteriou et al., 2005) led to a high bone mass phenotype that was not detectable until 5–9 months of age, past peak bone mass. These clinical and preclinical observations support a functional relationship between sympathetic tone and bone mass regulation, with highest relevance to age-related bone loss.

Further elucidation of the role of the SNS in normal physiology and skeletal pathologies is hindered by our limited understanding of both its physiology and its neurochemical function in the skeleton. We have previously reported that the norepinephrine transporter (NET), a pump that uptakes NE from the extracellular space, plays an important role in the regulation of bone remodeling (Ma et al., 2013), as global *Net* deletion results in low bone mass in mice. Although lack of NE reuptake by SNS terminals in bone would be expected to cause bone loss via increased NE spillover in the bone microenvironment, this low bone mass phenotype was unexpectedly accompanied by low skeletal NE content. According to the above model of skeletal-SNS interaction, this observed low NE bone content should promote bone gain. Investigating this contradictory result led us to show that NET is expressed not only in skeletal nerve terminals, but also in cells of the osteoblast lineage, and to demonstrate specific *Net* expression and NE uptake in differentiated osteoblasts *in vitro* (Ma et al., 2013). This work led us to hypothesize that NET has an extraneuronal role in bone to locally limit the action of NE on the skeleton, thereby buffering the catabolic function of the SNS on this organ. To further address this model, NE uptake by skeletal cells in the adult skeleton in vivo, as well as the skeletal distribution of NE releasing sympathetic nerve fibers relative to these cells needed to be demonstrated.

2. Results

2.1. Aging leads to increased basal NE content in the skeleton

Aging is associated with an increase in basal sympathetic tone in humans (Hart and Charkoudian, 2014; Iwase et al., 1991), a condition that might be partially responsible for the age-related decline in organ function (Paschalis et al., 2015; Zhou et al., 2008). Potential repercussions on the skeleton and bone mass remain unknown. Therefore, we first asked whether NE bone content differed between young and old mice. Using high-performance liquid chromatography, we detected a 29% increase in NE content/mg protein in whole tibia samples from 18-month versus 3-month-old mice (Fig. 1A). The amount of the catecholamine precursor L-dihydroxyphenylalanine (L-DOPA) in these tissues was not significantly different between 3 and 18-month-old animals whereas the ratio between DOPA/NE was higher in 3-month old animals, thus suggesting the higher skeletal NE in older animals is not due to increased sympathetic outflow (Fig. 1A). When NET uptakes NE into cells, a large proportion is converted to the metabolite dihydroxyphenylglycol (DHPG). The amount of DHPG was not different between 3 and 18-month-old animals, despite increased NE content in the 18 month-old group, leading to lower DHPG/NE ratio in 18-month-old mice (an indicator of reduced NE tissue metabolism). Since breakdown of NE into DHPG requires cellular uptake, this result further supports deficient uptake/metabolism during aging (Fig. 1B). In subsequent studies, a progressive increase in cortical bone NE content in aging mice (1 to 12 months of age) was also detected via high sensitivity NE ELISA (Fig. 1C). Therefore, aging is associated with an increase in cortical bone NE content that is not associated with a detectable increase in NE synthesis, and is concurrent with decreased catecholamine metabolism.

2.2. In vivo skeletal NET activity decreases with age

NET is well known to be expressed in presynaptic sympathetic neurons (Mandela and Ordway, 2006), but was also unexpectedly detected in neonate osteoblasts by immunohistochemistry, and in differentiated osteoblasts in vitro at both RNA and protein levels (Ma et al., 2013). These data, along with the known bone loss associated with aging, the low bone mass of *Net−/−* mice and the increased NE content in the bones of aged mice (Fig. 1A), led us to hypothesize that during aging, differentiated osteoblasts and/or osteocytes lose their capacity to uptake NE, leading to overt β2AR stimulation and bone loss. To address this hypothesis, we established a method to measure NET-mediated acute uptake of the radioligand [^{3}H]-NE in bone tissues of live adult mice. To ensure specificity of NE uptake by NET in these measurements, mice (n = 6–8) were pre-treated twice with the NET blocker reboxetine (i.p. 20 mg/kg BW) or sterile saline vehicle 60 and 30 min prior to administration of [^{3}H]-NE (10 μCi/kg BW) via tail-vein injection to avoid excess hepatic metabolism. The radioligand was allowed to circulate for 10 min, after which the animals were rapidly euthanized, and tibiae and femurs were harvested. Specific [^{3}H]-NE uptake via NET (AKA reboxetine-sensitive uptake) in cortical and marrow tissues was calculated as the difference between the vehicle-pretreated (total tissue uptake) and reboxetine-pretreated (non-NET uptake) groups, and normalized by tissue DNA content (as an indirect readout for cell number). Consistent with previous in vitro data showing NET expression and activity in differentiated osteoblasts (Ma et al., 2013), and despite some level of variability stemming from the multiple experimental steps involved, acute [^{3}H]-NE specific uptake was detected in bone tissue in vivo and was significantly higher in the cortex (enriched in mature osteoblasts and osteocytes) than in the marrow of 3-month-old mice (Fig. 1D). Moreover, a significant reduction in specific [^{3}H]-NE uptake was observed in the bone cortex of 9 versus 3-month-old mice, whereas no significant change across ages was detected in the marrow.

2.3. Net expression in cortical bone decreases with aging

In vivo specific NE uptake by cortical bone tissues, whose cellularity is comprised of > 90% osteocytes (Dallas and Bonewald, 2010), and uptake activity detected specifically in differentiated osteoblasts *in vitro* (Ma et al., 2013) suggested that cortical osteocytes might be the main site of NET uptake in vivo. We, therefore, measured NET expression in flushed femoral cortices of WT C57BL6 mice at different ages, from one month until 12 months of age, a time where bone loss is already significant in these mice (Ferguson et al., 2003). NET protein expression peaked at two months of age (near peak bone mass), followed by a reduction significant by 3 months (Fig. 1E). A similar pattern of expression across ages was observed at the RNA level, suggesting that age impacts the transcription of *Net*, rather than protein content or stability, in cortical bone osteocytes (Fig. 1F and SIA). The expression of the osteocyte marker gene *Sost* in these samples was not overtly affected by age (Fig. 1G and S1B). Taken together, these results indicate that NET gene and protein expression in cortical bone decreases with age.

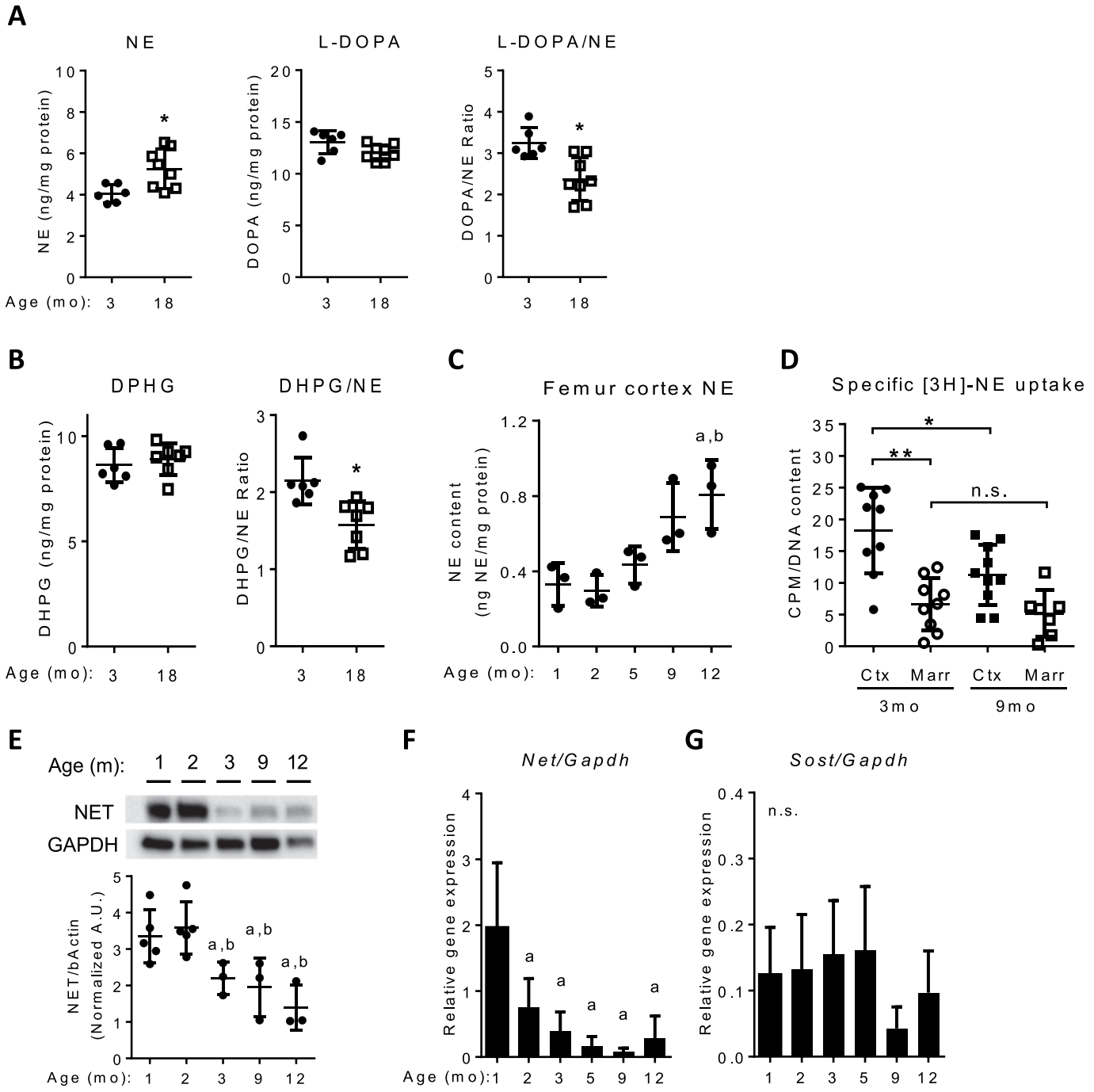

Fig. 1. In vivo skeletal NET expression and function decreases with age.

(A) Levels of norepinephrine (NE), L-DOPA, and L-DOPA/NE ratio in whole tibiae from young and aging mice, measured by HPLC and normalized to lysate protein concentration (n = 7–8 per group).

(B) Levels of DHPG and DHPG/NE ratio in whole tibiae from young and aging mice, measured by HPLC and normalized to lysate protein concentration (n = 7–8 per group).

(C) NE levels in femoral cortical tissues from mice of different ages, measured by ELISA and normalized to lysate protein concentration (n = 3/time point).

(D) In vivo reboxetine-sensitive acute specific uptake of [^{3}H]-NE radioligand in the femoral cortex and marrow of 3- and 9-month old mice, normalized to lysate DNA content (n = 6–8 per group).

(E) Representative Western blot and quantification of NET expression in flushed femoral cortical tissues from mice of different ages, normalized to reference gene GAPDH (n = 3–5 per group).

(F–G) Expression of *Net* (F) and *Sost* (G) in flushed femural cortices from mice of different ages, normalized to reference gene *Gapdh* (n = 3–6 per group).

Tissues were harvested from male C57BL6/J male mice of indicated age, with the cortex and marrow separated unless indicated otherwise. All results are shown as mean ± SD. Statistical analysis by two-tailed Student's *t*-test (A–B), or one-way ANOVA, $^*p < 0.05$; post-hoc Bonferroni statistical test for pair-wise significance (C–G), *a* $p < 0.05$ vs 1 month, *b* $p < 0.05$ vs 2 month.

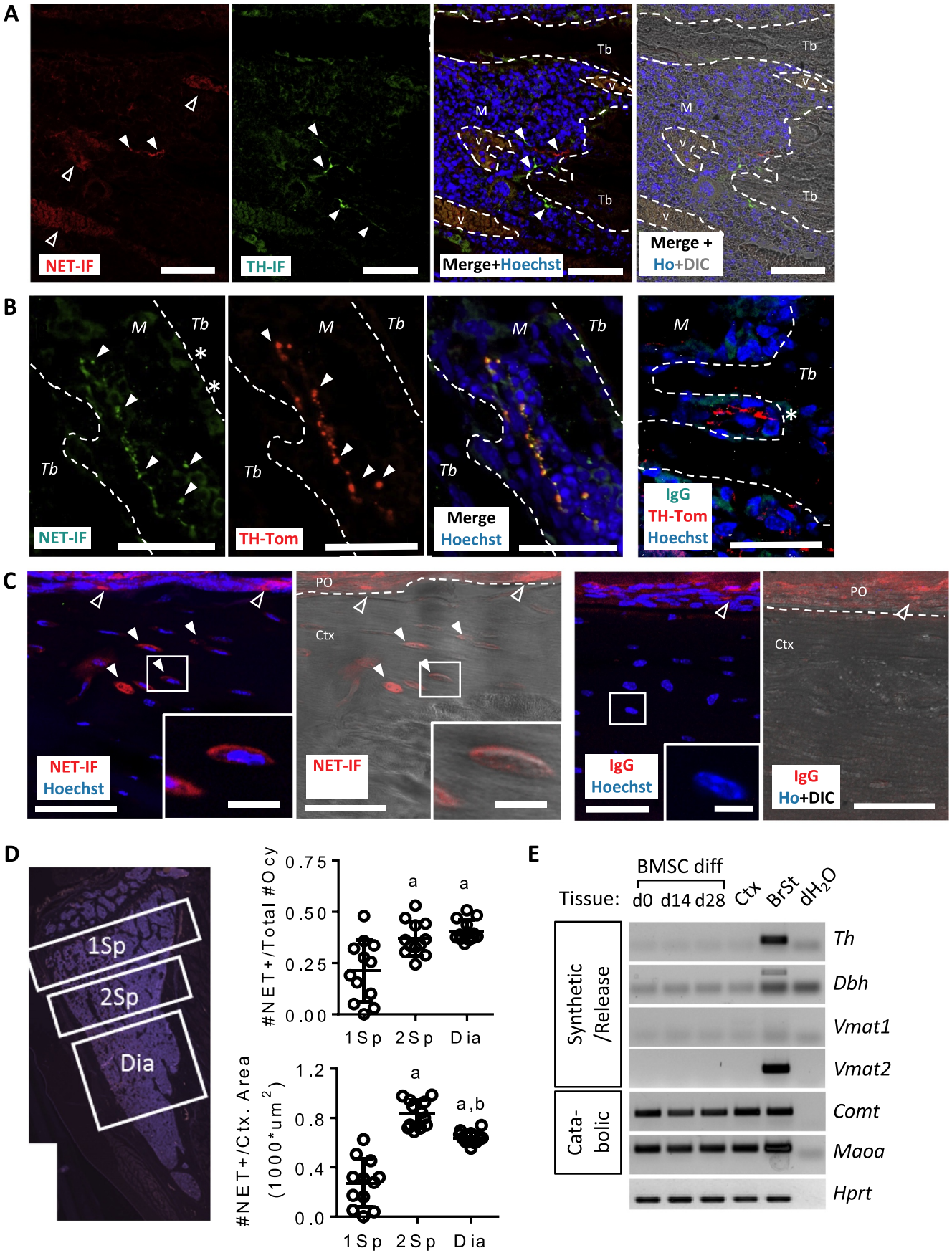

(caption on next page)

Fig. 2. NET immunofluorescence in bone tissues.
Legend: vessel (v), trabeculae (*Tb*), cortex (*Ctx*), marrow (*M*), periosteum (*PO*), *IF*: immunofluorescence, *DIC*: Differential interference contrast microscopy.
(A) Immunofluorescence images of fibers with NET (red) and TH (green)-immunostaining in tibial trabecular zone (closed arrowheads). Non-specific background fluorescence is visible in blood vessel erythrocytes (open arrowheads). Images are representative of 2 sections from 3 animals. Scale bars 50 μm.
(B) NET immunofluorescence (green, closed arrowheads) colocalization with TH-Tomato expression (red), and IgG primary antibody negative control in tibial diaphyseal cortex sections. Weaker signal is observed in cuboidal cells apposed to trabeculae (asterisks). Images are representative of 2 sections from 3 animals. Scale bar 50 μm. Inset: magnified matrix-embedded osteocytes, scale bar 20 μm.
(C) Max. intensity projection of NET-immunofluorescence (red, closed arrowheads, left images), and IgG primary antibody negative control (right images) in tibial diaphyseal cortex sections. Non-specific background fluorescence is observable in the periosteum (open arrowheads). Images representative of 2 sections from 3 animals, projections from 9 confocal optical sections through 10 μm depth. Scale bar 50 μm. Inset: magnified matrix-embedded osteocytes, scale bar 20 μm.
(D) Density of NET^+ osteocytes per total number of osteocytes or total cortex area per region in primary spongiosa (1Sp), secondary spongiosa (2Sp), or diaphysis (Dia). n = 4 animals, 3 sections per animal.
(E) Semi-quantitative RT-PCR of differentiating bone marrow stromal cells (BMSCs), tibial cortical tissues (Ctx), and brainstem (BrSt) for genes encoding enzymes related to catecholamine metabolism and synthesis.
All results are shown as mean ± SD. Statistical analysis by one-way ANOVA, post-hoc Bonferoni statistical test for pair-wise significance; *a* $p < 0.05$ vs 1Sp, *b* $p < 0.05$ vs 2Sp. (For interpretation of the references to color in this figure legend, the reader is referred to the web version of this article.)

2.4. NET is expressed in cortical osteocytes

Although we have previously detected NET tissue expression in the primary spongiosa of tibiae from post-natal day 2 pups (Ma et al., 2013), osteoblast-lineage NET expression in the adult skeleton had yet to be demonstrated. We thus investigated NET expression in adult bones using immunofluorescence. As expected, NET immunoreactivity was detected in fine fiber structures in the marrow of the adult tibia, among TH-positive nerve fibers (closed arrowheads) close to trabecular bone surfaces in the secondary spongiosa region (Fig. 2A), or colocalized with nerve fibers expressing the Tomato reporter driven by TH-Cre recombination (Fig. 2B). A weak signal was also detected in these high magnification images in osteoblast-like cells positioned against bone trabeculae, consistent with the previously described expression of NET in differentiated osteoblasts (asterisks in Fig. 2B). Most importantly, strong NET immunostaining was also detected in matrix embedded osteocytes in the tibial cortex of these mice (Fig. 2C), but not in trabecular osteocytes (not shown). Staining was mainly detected in the cell body of positive osteocytes, but not in osteocyte processes. NET expression was not uniform across all tibial cortical regions. Osteocytic NET expression was the highest in the cortical region adjacent to the secondary spongiosa and the diaphysis, while relatively sparse around the primary spongiosa/perichondrium (Fig. 2D).

Several observations support the specificity of the NET staining in these experiments. First, staining with this antibody was observed in the pericellular area of TH-positive adrenal medullary chromaffin cells, which are catecholaminergic neuroendocrine cells known to express NET at their surface (Fig. S2A, positive control). Second, replacement of the primary antibody against NET by a non-immune IgG did not label any neuronal structure nor osteocytes (Fig. 2C, right two panels), although some signal was observed in blood vessel erythrocytes (Fig. 2A, open arrow) and in the periosteum (Fig. 2C, open arrow) in both anti-NET and mouse IgG isotype groups. This similar pattern of expression between the anti-NET and mouse IgG isotype groups strongly suggests that this erythrocyte and periosteal staining is indeed background signal. The analysis of mice deficient for *Net* will be necessary to confirm this, however, the observation that NET immunoreactivity disappeared (along with TH immunoreactivity) in bone marrow neurons (but not osteocytes) in tibial sections from animals chemically sympathectomized with 6OHDA (Fig. S2B–E) further supports specificity of the anti-NET antibody.

In pre-synaptic neurons, NET reuptake serves a dual role: it limits synaptic NE signaling, and recycles NE for subsequent repackaging and re-release. In differentiating bone marrow stromal cells (BMSCs) and cortical bone tissues, expression of NE catabolic enzymes, including catechol-*O*-methyltransferase (*Comt*) and the peripheral isoform of monoamine oxidase (*Maoa*) was detected by RT-PCR. However, genes encoding enzymes for catecholamine synthesis, tyrosine hydroxylase (*Th*) and dopamine-β-hydroxylase (*Dbh*); or vesicular repackaging, vesicular monoamine transporters 1 and 2 (*Vmat1/2*) were not detected in differentiating BMSCs and bone cortex (Fig. 2E). Furthermore, expression of the catabolic enzyme gene *Maoa* decreased with age (Fig. S1C–D) whereas *Comt* expression was not changed, suggesting that aging affects NE catabolic pathways downstream of NET as well. These results point to osteocytes and cortical bones as extraneuronal sites of NE uptake and catabolism, but not synthesis.

2.5. Whole-mount distribution of sympathetic nerves in adult long bones

Previous studies have documented the presence of TH^+ fibers in bone (Chartier et al., 2018; Mach et al., 2002; Bataille et al., 2012; Bjurholm et al., 1988). A question raised by the finding of NE uptake activity in cortical bone was thus whether SNS fibers were located in this bone compartment. To investigate the distribution of sympathetic tyrosine hydroxylase-positive (TH^+) nerve fibers in long bones, we generated transgenic reporter mice overexpressing a tdTomato fluorescent reporter protein in TH-Cre^+ cells (TH-Tomato) (Madisen et al., 2010). In order to visualize long TH^+ fibers in and around the cortical envelop volume, we applied bone CLARITY optical clearing and whole mount light sheet microscopy imaging techniques (Yang et al., 2014; Greenbaum et al., 2017) to clear whole femurs hemi-sectioned longitudinally (see Materials and Methods, Fig. S3 and Fig. 3A). In order to differentiate tissues, Hoechst stain (blue) and tissue autofluorescence (false color gray) were used to approximate location of the TH-Tomato signal (red). Using this approach, SNS fibers were grossly observed in the diaphyseal region in 3D reconstruction tissue and top-down maximum intensity projection (MIP) of the tissues (Fig. 3B). To determine the tissue-level location of SNS fibers, digital sections of the entire tissue images were generated. TH-$Tomato^+$ signals were observed in the periosteum area, as previously reported (Chartier et al., 2018), but also within compact cortical bone (Fig. 4A and B). Digital coronal sections of the diaphysis at all levels of cortex studied confirmed TH-tomato signals within the compact bone cortical envelop (Fig. 4C).

3. Discussion

The amount of endogenous NE released by sympathetic nerves is modulated presynaptically by NET, whose NE uptake function accounts for 80–90% of NE released by central and peripheral neurons (Schömig et al., 1989; Galli et al., 1995; Caron et al., 2000). NE reuptake thus constitutes an important negative feedback mechanism to limit the duration of sympathetic signaling and to replenish NE stores in sympathetic nerve fibers (Galli et al., 1995). The low bone mass phenotype of mice globally deficient for *Net* indicated that this transporter is important for bone remodeling (Ma et al., 2013). However, how NET modulates bone mass remains unknown, although in vitro evidence suggested that differentiated osteoblasts might contribute to NE uptake in bone. In this study, we show: 1) this transporter is expressed in vivo

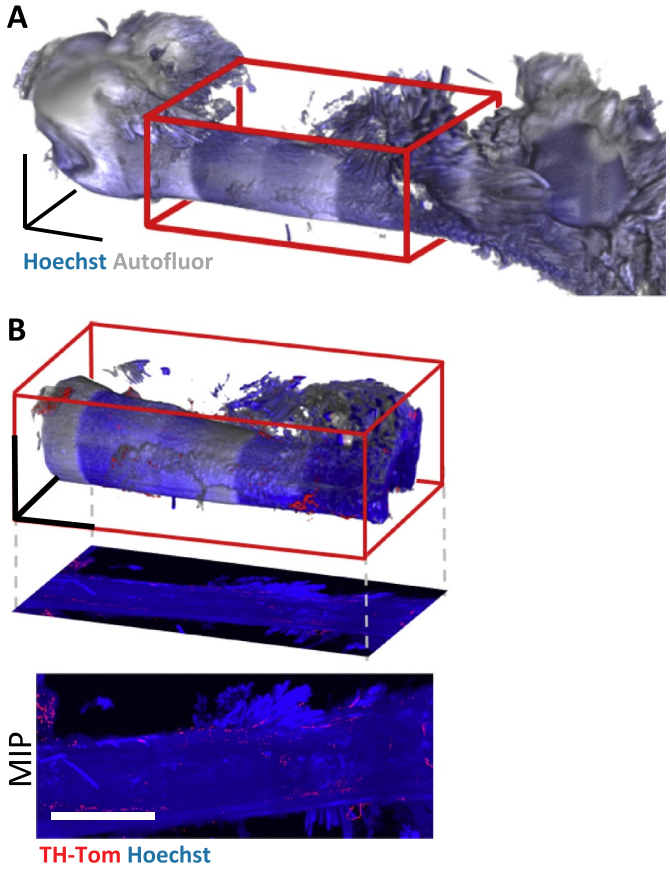

Fig. 3. Whole-mount imaging of TH^+ sympathetic nerves in bone.
(A) Representative 3D reconstruction of femur hemisection from light sheet imaging of entire tissue. Diaphysis region is highlighted (red box). Image shows Hoechst fluorescent staining (blue) and FITC-autofluorescence (false color gray). Scale axis bars 500 μm.
(B) Boxed diaphysis region from 3D femur hemisection reconstruction, and top-down maximum intensity projection (MIP) of boxed region. Tissue imaged from Hoechst (blue) and FITC-autofluorescence (false color gray), and sympathetic nerves by TH-tdTomato fibers (TH-Tom, red). Scale axis bars 500 μm. (For interpretation of the references to color in this figure legend, the reader is referred to the web version of this article.)

in adult mouse cortical osteocytes; 2) the adult cortical bone is a site of in vivo NET-mediated NE uptake; and 3) sympathetic fibers are distributed within the cortical bone envelope; and 4) for the first time provide evidence for a reduction in NET expression and function in mouse bones during aging. Together, these data support the model whereby NE uptake by NET in cortical osteocytes buffers endogenous NE released by sympathetic nerve fibers, and suggest that failure of this homeostatic system might contribute to age-related bone loss, although this latter point will need to be addressed by in vivo loss-of-function experiments.

Although pharmacological βAR stimulation induced bone loss in mice (Elefteriou et al., 2005; Ma et al., 2011), neither short-term chronic pharmacologic blockade of NET alone (by the antagonist reboxetine), nor increased endogenous NE release (by a chronic immobilization stress protocol) impacted bone mass in young mice. However, chronic stress led to a significant loss of bone mass when combined with NET blockade with reboxetine (Ma et al., 2013). These results were the first to suggest that NET protects the skeleton from the catabolic action of NE released from activated sympathetic fibers and that conditions associated with impaired NET function and increased SNS outflow might lead to bone loss. Aging might represent such condition. Overall, high NE extracellular levels can be due to either increased synthesis and release, or decreased metabolism and uptake. During aging, increased cardiovascular NE spillover has been shown to stem from decreased NET capacity (Esler et al., 1995). We show in this study a similar age-related change in the skeleton, with resting NE levels higher in bones from older mice. The normal levels of the catecholamine precursor L-DOPA and higher L-DOPA/NE ratio (a commonly used sensitive measurement of altered catecholamine metabolism (Vincent et al., 2004)) in bone from younger mice suggested the observed increase in bone NE was unlikely from increased synthesis. On the other hand, there was no difference in levels of the catecholamine metabolite DHPG in older mice despite higher NE levels, resulting in a lower DHPG/NE ratio, suggesting deficits in NE uptake/metabolism in vivo. This conclusion is further supported by the reduction in acute in vivo [^{3}H]-NE uptake in the bone of aged animals, highlighting a deficit in reuptake function during aging. Furthermore, decreased *Maoa* expression in skeletal tissues from aged animals may also contribute to the observed increase in NE bone content, yet decreased DHPG/NE ratio, seen during aging. Lastly, the observation by Chartier et al. (2018) that skeletal sympathetic nerve fiber density decreases with aging strengthens the idea that the increase in NE bone content during aging predominantly stems from abnormalities in NE uptake or catabolism instead of NE synthesis or release. These new in vivo results, along with the expression of NE catabolic enzymes in osteocyte-like cultures, thus support the hypothesis that osteocytes function as a catabolic sink for NE in bone, and that this capacity is diminished with age. However, at this whole-tissue resolution, it was not possible to determine whether the decrease in NET expression and function with age was caused by the natural decrease in osteocyte density with age (Tiede-Lewis et al., 2017) or by an intrinsic cell-autonomous reduction in *Net* expression in “old” osteocytes.

Expression of NET in bone tissues was previously described only in trabecular osteoblasts of postnatal day 3 mice, which do not yet have a significant density of osteocytes (Ma et al., 2013). In the context of data suggesting a deleterious impact of sympathetic nerve signaling on bone during aging, it was necessary to assess NET expression and function in adult tissues. Through immunofluorescence microscopy methods, we were able to identify NET expression in adult bone-embedded cortical osteocytes, a result consistent with higher NET uptake activity in flushed femurs versus marrow. A majority of NET^+ osteocytes were observed in the periosteal cortical envelope, consistent with the observed location of SNS fibers and the lower turnover of cortical versus trabecular bone. These results thus suggest that osteocytes modulate, via uptake of NE, the communication between sympathetic nerves and $\beta2AR^+$ osteoblasts, although it remains unclear which effector cell in the osteoblast lineage (osteoblasts, osteocytes, or both) is the target of sympathetic nerves. Isoproterenol (ISO) stimulation of the β2AR affects bone through both arms of the bone remodeling process, inhibiting osteoblast proliferation via cell-autonomous circadian genes *Per* and *Cry* (Fu et al., 2005), and stimulating RANKL production to promote osteoclast differentiation (Elefteriou et al., 2005). These two actions cannot occur within the same cell, as the anti-proliferative action of NE relates to pre-osteoblasts, whereas osteocyte-derived RANKL plays a predominant role in bone remodeling (Xiong et al., 2011). Furthermore, these two cell types inhabit different locations in bone: pre-osteoblasts are located near the endosteal bone surface and migratory (Yamashita et al., 2010), whereas osteocytes are embedded and stationary in the calcified bone matrix. Localization of SNS fibers near perivascular hematopoietic (Katayama et al., 2006) and mesenchymal stem cell niches (Méndez-Ferrer et al., 2010; Cole et al., 2015) were previously reported. However, only a few reports (Mach et al., 2002; Calvo, 1968) suggest a close vicinity with osteoblast-lineage cells. Whether the primary target of endogenous NE among bone-forming cells is the osteoblast or the osteocyte thus remains unclear.

Compared to previous reports, our study provides an independent analysis of sympathetic innervation of the skeleton, using an alternative method based on TH-Cre-mediated fluorescent signals and 3D bone CLARITY imaging. Bone CLARITY has been previously applied with

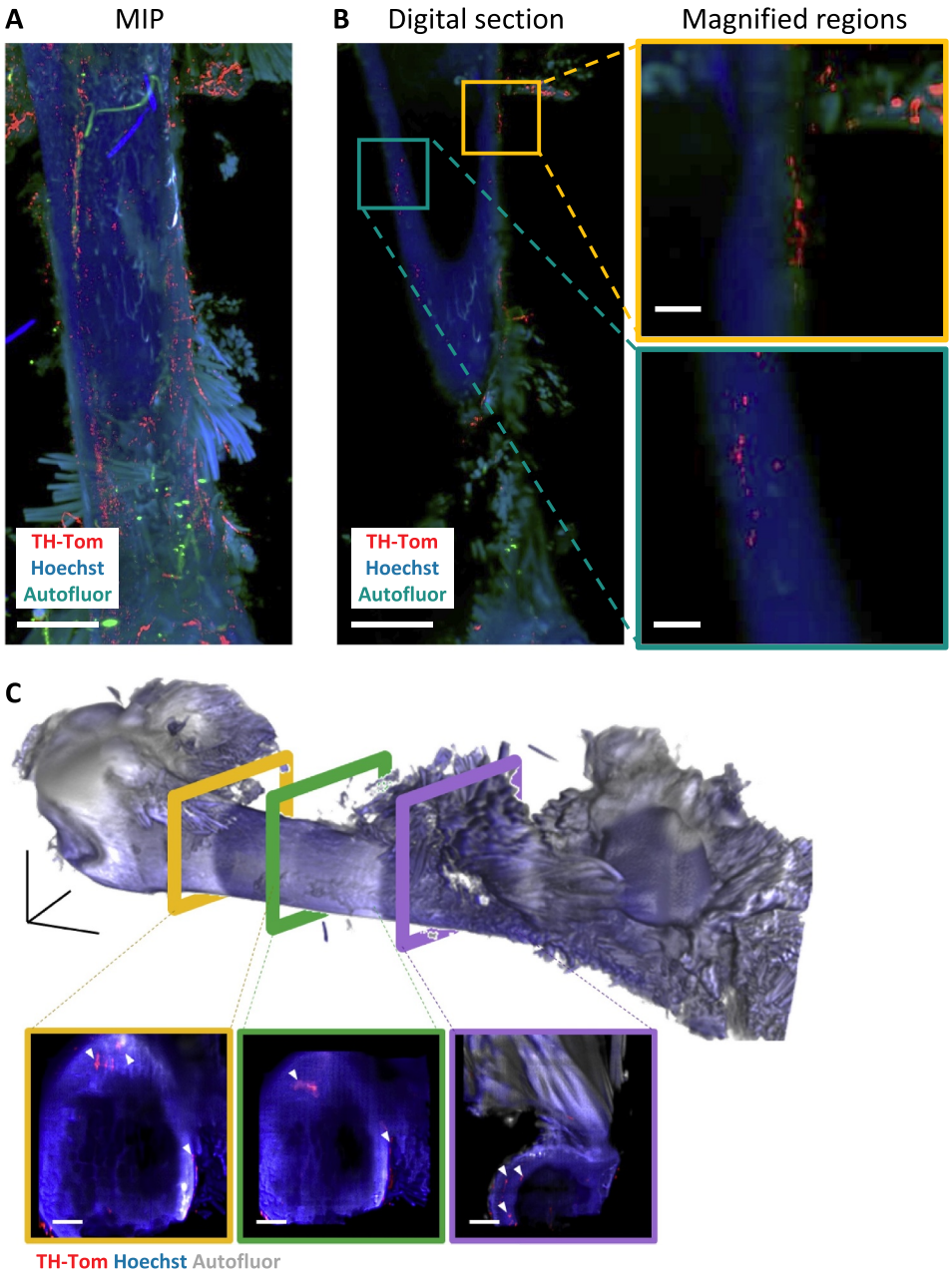

Fig. 4. TH$^+$ fibers in cortex sections of 3D reconstructed femurs
(A) Top-down maximum intensity projection (MIP) of boxed diaphysis region from Fig. 3 showing TH-Tomato signal (red), Hoechst fluorescent staining (blue), and FITC-autofluorescence (green).
(B) Top-down MIP digital section of 10 *Z*-frames (36 μm) of the tissue in (A). Scale bars 400 μm. Highlighted regions (yellow and green boxes) shown in magnified panels, scale bar 100 μm.
(C) Coronal digital sections, indicated by colored frames (yellow, green, and purple) on 3D reconstructed femur hemisection. Image constructed from Hoechst fluorescent staining (blue) and FITC autofluorescence (false color gray). Scale axis bars 500 μm. Digital tissue cross-sections 50 μm thick, show red TH-Tom fluorescent signal located within cortical/periosteal tissues (arrowheads), scale bar 100 μm.
All images are representative of femurs hemisections from 3 animals. (For interpretation of the references to color in this figure legend, the reader is referred to the web version of this article.)

success to imaging rare cell populations in whole mouse bones (Greenbaum et al., 2017). Here, we applied this technology for visualizing long sympathetic nerves in adult femurs, with a focus on intracortical distribution. We were able to confirm innervation of the periosteum and to detect innervation of the femoral cortices, but were not able to detect fine nerve terminals reaching osteocytes. Limitation associated with the cytoplasmic expression of the tdTomato reporter used in this study may account for the lack of detection of fine fibers within cortical bone, as the thin diameter of sympathetic nerve terminals may be insufficient for significant cytoplasmic fluorescent protein diffusion and detection. It is also possible that other mechanisms aside from direct osteocyte-neuronal interactions are involved in the effect of NE on bone remodeling. Studies focused on the adipose tissue indicated that only approximately 4–12% of inguinal fat pad adipocytes are in direct contact with SNS fibers (Zeng et al., 2015), with inter-adipocyte gap junctions shown to propagate secondary messenger molecules like cAMP between adjacent cells. The inter-osteocyte connectivity and the connections between osteocytes and osteoblasts make this putative signaling mechanism possible in bone, as inter-osteocyte communication has already been demonstrated to translate mechanical strain signaling to adjacent cells (Robling et al., 2008). In addition, the gap junction protein Connexin43, encoded by *Gja1*, can form gap junctions between adjacent cells, and expression of a dominant-negative *Gja1* mutant resulted in increased cortical bone (Xu et al., 2015; Shen et al., 2015). It is thus plausible that inter-osteocyte communication via gap junctions following β2AR stimulation in osteocytes could mediate secondary messenger diffusion, and contribute to propagating signals from single stimulated cells across the larger osteocyte network to eventually impact bone remodeling. In any case, the data presented herein provide a strong incentive to assess the in vivo functional relevance of NET-mediated NE uptake by osteocytes and its impact on bone remodeling during bone acquisition and aging.

4. Materials and methods

4.1. Mice

Wild-type male C57BL6/J mice (JAX#000664) and *Th-Cre* mice (JAX#008601) on a C57BL/6J background were purchased from the Jackson Laboratory, and allowed to acclimate to the environment for at least one week prior to experimentation. ROSA-LSL-tdTomato reporter mice (Ai9, JAX#007905) on a C57BL/6 J background were a generous gift from Dr. Dongsu Park. *Th-Cre*; *ROSA-LSL-tdTomato* (*Th-Tom*) mice were generated by our laboratory, and genotype was confirmed by PCR (primers Table S1.) Animals were housed 2–5 per cage, kept on a 12 h light-dark cycle in a temperature-controlled environment (22 °C), and had ad libitum access to water and standard chow. This study used male mice since previous studies (Ma et al., 2013) in $Net^{-/-}$ mice showed a bone phenotype only in males. All animal procedures were performed according to protocols approved by the Institutional Animal Care and Use Committee at Baylor College of Medicine.

4.2. Catecholamine measurements

Male mice (3 and 18 month-old) were sacrificed for high-pressure liquid chromatography (HPLC) measurements of catecholamines. Tibiae were cleaned of connective tissues and clipped at the epiphyses. Marrow was separated from cortical bone via centrifugation at 5000*g* for 2 min, and snap frozen in liquid nitrogen. Frozen tissues were crushed in a mortar and pestle, resuspended in 100 µl of 0.1% reduced L-glutathione (Cat#G4251, Sigma-Aldrich) in 0.1 M Tris pH 8.0 to protect from oxidation. Norepinephrine, L-dihydroxyphenylalanine (L-DOPA), and dihydroxyphenylglycol (DHPG) quantification was determined by HPLC at the Neurochemistry Core Lab, Vanderbilt University Center for Molecular Neuroscience Research (Nashville, TN), using methods previously described (Mai et al., 2014). Sample protein contents were measured by BCA assay (Cat#23225, Thermofisher) and used to normalize catecholamine levels.

Mice aged 1, 2, 5, 9, and 12 months were sacrificed for NE ELISA measurements. Tissues were prepared similarly to those for HPLC measurements. Frozen bone powder was resuspended in glutathione tissue extraction buffer (0.01 N HCl, 0.15 mM EDTA, 0.1% reduced glutathione), and neutralized with 10% volume of 1.0 M Tris pH 8.0 prior to NE ELISA. NE levels were measured by high sensitivity NE ELISA kit (Cat#NOU39-K01, Eagle Biosciences) according to manufacturer's protocol. An aliquot of tissue suspended in extraction buffer was used to quantify protein concentration, and used to normalize NE measurements.

4.3. Specific [^{3}H]-NE in vivo uptake

In vivo uptake assays were conducted in 6-week old C57BL6/J male mice. Animals were pretreated twice at $t = -1$ h and -0.5 h with either sterile saline vehicle or Reboxetine mesylate (Cat#1982, Tocris) at 20 mg/kg intraperitoneally. This concentration was chosen based on previous studies with reboxetine tissue binding (Rasmussen and Nedergaard, 2003; Haenisch et al., 2009) and reported anti-mobility effects of the drug (Wong et al., 2000; Dostert et al., 1997). Then, 0.2 µCi L-[7-^{3}H]-NE (Cat#NET377250UC, Perkin Elmer), approximately 10 nmol in 200 µl warmed saline, was administered via tail vein injection. After 10 min of radioligand circulation, animals were euthanized by cervical dislocation, and tibia and femur were harvested. Bones were cleaned of connective tissues and clipped at the epiphyses. Marrow was separated from cortical bone via centrifugation at 5000*g* for 2 min, and snap frozen in liquid nitrogen. Frozen cortices were crushed with a mortar and pestle. Marrow and powdered cortical tissues were incubated in lysis buffer (0.15 mM EDTA, 20 mM Tris pH 7.5, 0.05% Triton-X100), and radioligand was quantified by scintillation counting. An aliquot of tissue lysate resuspended in buffer was used to measure tissue DNA content by Picogreen dsDNA assay kit (Cat#P7589, Thermofisher), used to normalize radioligand tissue quantities to cell density. Specific uptake was calculated using the following formula: $specific\ uptake = \frac{CPM_{Veh}}{dsDNA_{Veh}} - \frac{CPM_{Rebox}}{dsDNA_{Rebox}}$.

4.4. Cell culture

Bone marrow was extracted from long bones of 2–4 month-old C57BL6/J mice by centrifugation, as previously described (Campbell et al., 2012), and was plated on 6-well tissue culture treated plates in α-MEM (+glutamate, +nucleosides), supplemented with 10% fetal bovine serum and 100 U/ml penicillin/streptomycin at seeding density of 2×10^5 cells/well for three days. At that time, non-adherent cells were washed, and adherent bone marrow stromal cells (BMSCs) were differentiated in osteogenic medium (α-MEM, 10% FBS, pen/strep with 50 µg/ml L-ascorbic acid and 5 mM β-glycerophosphate), changed every 2 days, until harvested for assays at indicated time points.

4.5. Gene expression assays and RT-PCR

Tibia and brainstem were harvested, cleaned of connective tissues, and flash frozen in liquid nitrogen. Marrow and cortex tissue were separated (where applicable) via centrifugation at 5000*g* for 2 min, and snap frozen in liquid nitrogen. Frozen tissues were crushed via mortar and pestle. Total RNA was extracted from tissue powder and differentiated BMSCs using TRIzol (Cat#15596026, Thermofisher). Contaminating genomic DNA was digested with DNAse I (Cat#18068015, Thermofisher). cDNAs were synthesized from 1 µg RNA using high capacity cDNA reverse transcription kit (Cat#4368814, Thermofisher) according to the manufacturer's instructions. Estimating 80% reverse transcription efficiency, 25 ng cDNA was used in each reaction. Gene expression was quantified by qRT-PCR using iTaq Universal Probes Supermix (Cat#1725131, Bio-rad) or iQ SYBR Green Supermix (Cat#1708882, Bio-rad) according to manufacturer's instruction for Taqman and SYBR probes, respectively. Target gene expression ratios were quantified using a standard curve of cDNA from similar tissues and normalized with references genes *Gapdh* and *Hprt*. RT-PCRs of catecholaminergic genes were performed with primers designed for SYBR qRT-PCR, then separated and visualized on a 1% agarose gel. All SYBR and RT-PCR primer sequences and thermocycler protocols are provided in the Supplementary Data (Table S1). SYBR primer specificity for target gene amplification was confirmed by the presence of a single peak on the melt curves.

4.6. Western blot analysis

Femurs were dissected and cleaned of connective tissues and clipped at the epiphyses. Marrow was separated from cortical bone via centrifugation at 5000*g* for 2 min, and snap frozen in liquid nitrogen. Frozen femur cortices were crushed in a mortar and pestle. Protein was extracted from marrow and crushed cortex tissue by RIPA buffer extraction with protease inhibitor cocktail (Cat#P8340, Sigma-Aldrich), and concentrations quantified by BCA assay. Total of 15 µg protein was denatured with 2.5% β-mercaptoethanol, separated by SDS-PAGE on a 4–15% gel, and transferred onto a PVDF membrane. Membranes were blocked with 5% nonfat milk powder in TBS 0.05% Tween-20 (TBS-T) at RT for 30 min. For age-dependent NET expression experiments, mouse anti-NET (Cat#NET05-2, Mab Technologies) and rabbit anti-GAPDH (Cat#2118, Cell Signaling Technology) primary antibodies were incubated at 4 °C overnight diluted 1:500 and 1:2000 in blocking buffer, respectively. For confirmation of 6OHDA chemical sympathectomy, rabbit anti-TH (Cat#AB152, Millipore) and rabbit anti-GAPDH (Cat#2118, Cell Signaling Technology) primary antibodies were incubated at 4 °C overnight diluted 1:100 and 1:2000 in blocking buffer, respectively. Membranes were washed with TBS-T and

incubated for 1 h at RT with HRP-conjugated secondary goat anti-mouse antibody (Cat#sc-2005, Santa Crus) or HRP-conjugated goat anti-rabbit antibody (Cat#12-348, Millipore) diluted 1:10,000 in blocking buffer. Membranes were then washed and developed using ECL reagent (Cat#68835, Cell Signaling Technologies) on autoradiography film. Band intensities were quantified using ImageJ, normalized with respective β-actin loading control, and standardized with an identical internal positive control present on both gels.

4.7. Mouse tissue immunofluorescence

Femur and tibia were dissected from 6-week old males, fixed in 4% paraformaldehyde overnight at 4 °C, and decalcified with daily changes of 0.5 M EDTA pH 8.0 at 4 °C for 72 h. Tissues were then dehydrated in graded series of ethanol, cleared in xylenes, embedded in paraffin, and sectioned. Tissue sections were deparaffinized with xylenes, and rehydrated through graded ethanol baths. Antigen retrieval was performed on sections by incubating slides in retrieval buffer (10 mM Tris, 1 mM EDTA, 0.05% Tween-20, pH 9.0) for 30 min at 90 °C, and allowed to cool in buffer for 30 min, and proceeded to immunostaining.

Kidney and adrenal glands were dissected from 6-week old males, removed of excess perirenal fat, and fixed in 4% paraformaldehyde overnight at 4 °C. Tissues were cryoprotected through 48 h incubation in 30% sucrose, and embedded in OCT for cryosectioning. Tissue sections were dried at RT for 1 h, and rehydrated in PBS to remove excess OCT, and proceeded to immunostaining.

All tissue sections to be immunostained were permeabilized with 0.1% Triton, blocked with 5% normal goat serum 0.05% Tween in PBS, and incubated with primary antibodies: mouse anti-NET (Cat#NET05-2, Mab Technologies) or rabbit anti-TH (Cat#AB152, Millipore), or mouse IgG1 isotype control (Cat#MAB002, R&D Biosystems) at 1:500 dilution in blocking solution at 4 °C overnight. Slides were washed and incubated with secondary antibody goat anti-mouse IgG Alexafluor594 conjugate (Cat#115-587-003, Jackson Immuno) or anti-rabbit IgG Alexafluor488 conjugate (Cat#111-547-003, Jackson Immuno) at 1:1000 dilution in blocking solution at RT for 3 h. Sections were washed, stained with nuclear stain Hoechst (Cat#H3569, Thermofisher), and mounted. Fluorescent and bright-field Differential Interference Contrast (DIC) images were acquired using a Nikon A1R-s confocal microscope with a 40× Plan Fluor/0.75 NA objective. Images were acquired with identical laser intensity and camera exposures, and processed identically with NIS Elements Viewer 4.20 (Nikon Instruments Inc., Melville NY). A total of n = 4 animals, 4 tibial sections per animal, 2 frames per each were analyzed in ImageJ. The observer was blinded to the identity of images to eliminate bias.

4.8. 6OHDA Chemical sympathectomy

The chemical sympathectomy protocol was adapted from (Katayama et al., 2006). A total of 18 4-week old male mice, 9 treatment, 9 vehicle controls, were randomized and weighed. Animals were administered two doses of L-6-hydroxy-DOPA HCl (6OHDA, Cat#H4381, Sigma-Aldrich) in sterile saline vehicle via intraperitoneal injection at the following concentrations: day 0 at 100 mg/kg body weight, and day 2 at 250 mg/kg body weight. Animals were weighed and sacrificed on day 5.

4.9. Bone CLARITY protocol

The protocol for processing and clearing bone tissues for whole-mount imaging was adapted from (Greenbaum et al., 2017), and summarized in Fig. S3. Femur were harvested from 6-week old male mice, bluntly stripped of overlying muscles and connective tissues, and fixed in 4% paraformaldehyde overnight at 4 °C. Bones were decalcified in daily changes of 0.5 M EDTA pH 8.0 at 4 °C for 72 h to increase light and reagent penetration. Tissues were then washed with 2 h RT incubation in PBS, cryoprotected in 30% sucrose at 4 °C overnight, and cryoembedded in OCT mounting medium for hemisectioning to improve access of reagents and stains to the bone medulla. Hemisectioned tissues were thawed and washed of OCT in PBS, and incubated in A4P0 acrylamide solution containing 4% acrylamide (Cat#A4058, Sigma-Aldrich), 0.25% VA-044 photoinitiator (Cat#27776-21-2, Wako Chemicals) in PBS at 4 °C overnight. Tissues were degassed via gas exchange by bubbling N_2 through the solution under a vacuum. The acrylamide hydrogel was polymerized by incubation for 6 h in a 37 °C water bath. The hydrogel supports the protein structures through the subsequent delipidation and washing steps.

Tissue lipids, a major source of light scattering, were washed away by shaking samples in 8% SDS in 1× PBS at 37 °C for 3 days, with daily changes of SDS solution. Heme and its porphyrin metabolites, a major source of tissue autofluorescence (Greenbaum et al., 2017), were removed by incubating tissues in 25% amino alcohol Quadrol (N,N,N′,N′-tetrakis(2-hydroxypropyl) ethylenediamine) (Cat#122262, Sigma-Aldrich) in PBS at 37 °C for 2d. Finally, tissues were washed in PBS for 24 h then stained with Hoechst (Cat#H3569, Thermofisher). Tissues were then embedded into 1% agarose-PBS, and cleared by immersion in Refractive Index Matching Solution (RIMS), comprising of Histodenz (Cat#D2158, Sigma-Aldrich) solution in PBS, through daily stepwise incubation of RIMS with index refraction RI = 1.38, 1.43, and finally 1.48 as recommended for bone (Yang et al., 2014).

4.10. Light sheet imaging

Tissues were imaged using a Zeiss LightSheet Z.1 side plane illumination microscope with an N-Achroplan 5×/0.13 objective. Before imaging, samples were placed in the LightSheet chamber filled with RIMS 1.48 for at least 1 h, allowing equilibration between the RIMS solution and sample. To image the entire bone, we acquired multiple *Z*-stack tiles with 15% overlap. Samples were imaged with a frame rate of 22 frames/s at a depth of 16 bits, with continuous motor drive through the Z-plane of the tissue. Tissues were excited by alternating left and right light sheets, and acquired images were merged using Gaussian merge function in the Zen software (Zeiss, Germany). All tissue samples were imaged using the same laser power and duration.

4.11. Image reconstruction and analysis

The sampled voxel size for a 5× objective was $0.92 \times 0.92 \times 9\,\mu m^3$, and generated approximately 300 GB per sample. After acquisition, the data sets were subset to voxel sizes $3.6 \times 3.6 \times 9\,\mu m^3$ for faster processing. Tile Z-scans of the images were stitched using the Arivis Vision4D software (Arivis AG, Washington DC), exported into Z-stack.tiff images for each color channel. The data was reconstructed by TIFF import in the Imaris v8.0 software (Bitplane, Concord MA), and image dimensions were corrected based on the original data set.

4.12. Statistical analysis

All statistical analyses were performed using Prism version 6 (GraphPad, La Jolla CA). Results are shown as mean ± standard deviation. Unless indicated otherwise, statistical comparisons using unpaired two-tailed Student's *t*-test for two-group comparisons, or one-way ANOVA followed by Bonferroni post hoc correction unless otherwise stated. For all analyses, $p < 0.05$ was considered statistically significant.

Supplementary data to this article can be found online at https://doi.org/10.1016/j.bonr.2018.11.002.

Declaration of interests

The authors declare no conflicts of interest.

Funding

The work reported in this article was supported by the National Institute of Aging of the National Institutes of Health (Bethesda, MD) under grant 1R01AG055394 (FE). The Vanderbilt Neurochemistry Core is supported by the EKS NICHD of the NIH under Award #U54HD083211.

Transparency document

The Transparency document associated with this article can be found, in online version.

Acknowledgements

We would like to thank Dr. Ginger Milne (Vanderbilt University Medical Center Neurochemistry Core lab) for assistance in quantifying bone catecholamines, and Jason Kirk and Dr. Chih-Wei Hsu (Baylor College of Medicine, Baylor Optical Imaging and Vital Microscopy Core) for assistance with microscopy.

References

Bataille, C., Mauprivez, C., Haÿ, E., et al., 2012. Different sympathetic pathways control the metabolism of distinct bone envelopes. Bone 50 (5), 1162–1172. https://doi.org/10.1016/J.BONE.2012.01.023.

Bjurholm, A., Kreicbergs, A., Terenius, L., Goldstein, M., Schultzberg, M., 1988. Neuropeptide Y-, tyrosine hydroxylase- and vasoactive intestinal polypeptide-immunoreactive nerves in bone and surrounding tissues. J. Auton. Nerv. Syst. 25 (2–3), 119–125.

Bonnet, N., Gadois, C., McCloskey, E., et al., 2007. Protective effect of beta blockers in postmenopausal women: influence on fractures, bone density, micro and macroarchitecture. Bone 40 (5), 1209–1216. https://doi.org/10.1016/j.bone.2007.01.006.

Calvo, W., 1968. The innervation of the bone marrow in laboratory animals. Am. J. Anat. 123 (2), 315–328. https://doi.org/10.1002/aja.1001230206.

Campbell, J.P., Karolak, M.R., Ma, Y., et al., 2012. Stimulation of host bone marrow stromal cells by sympathetic nerves promotes breast cancer bone metastasis in mice. PLoS Biol. 10 (7), e1001363. https://doi.org/10.1371/journal.pbio.1001363.

Caron, M.G., Xu, F., Gainetdinov, R.R., et al., 2000. Mice lacking the norepinephrine transporter are supersensitive to psychostimulants. Nat. Neurosci. 3 (5), 465–471. https://doi.org/10.1038/74839.

Chartier, S.R., Thompson, M.L., Longo, G., Fealk, M.N., Majuta, L.A., Mantyh, P.W., 2014. Exuberant sprouting of sensory and sympathetic nerve fibers in nonhealed bone fractures and the generation and maintenance of chronic skeletal pain. Pain 155 (11), 2323–2336. https://doi.org/10.1016/j.pain.2014.08.026.

Chartier, S.R., Mitchell, S.A.T., Majuta, L.A., Mantyh, P.W., February 2018. The changing sensory and sympathetic innervation of the young, adult and aging mouse femur. Neuroscience. https://doi.org/10.1016/J.NEUROSCIENCE.2018.01.047.

Cole, S.W., Nagaraja, A.S., Lutgendorf, S.K., Green, P.A., Sood, A.K., 2015. Sympathetic nervous system regulation of the tumour microenvironment. Nat. Rev. Cancer 15 (9), 563–572. https://doi.org/10.1038/nrc3978.

Dallas, S.L., Bonewald, L.F., 2010. Dynamics of the transition from osteoblast to osteocyte. Ann. N. Y. Acad. Sci. 1192, 437–443. https://doi.org/10.1111/j.1749-6632.2009.05246.x.

Dénes, Á., Boldogkoi, Z., Uhereczky, G., et al., 2005. Central autonomic control of the bone marrow: multisynaptic tract tracing by recombinant pseudorabies virus. Neuroscience 134 (3), 947–963. https://doi.org/10.1016/j.neuroscience.2005.03.060.

DiGirolamo, D.J., Clemens, T.L., Kousteni, S., 2012. The skeleton as an endocrine organ. Nat. Rev. Rheumatol. 8 (11), 674–683. https://doi.org/10.1038/nrrheum.2012.157.

Dostert, P., Benedetti, M.S., Poggesi, I., 1997. Review of the pharmacokinetics and metabolism of reboxetine, a selective noradrenaline reuptake inhibitor. Eur. Neuropsychopharmacol. 7 (Suppl 1(1)), S23–S35. discussion S71–3. https://doi.org/10.1016/S0924-977X(97)00417-3.

Eastell, R., O'Neill, T.W., Hofbauer, L.C., et al., 2016. Postmenopausal osteoporosis. Nat. Rev. Dis. Prim. 2, 16069. https://doi.org/10.1038/nrdp.2016.69.

Elefteriou, F., Ahn, J.D., Takeda, S., et al., 2005. Leptin regulation of bone resorption by the sympathetic nervous system and CART. Nature 434 (7032), 514–520. https://doi.org/10.1038/nature03398.

Esler, M.D., Thompson, J.M., Kaye, D.M., et al., 1995. Effects of aging on the responsiveness of the human cardiac sympathetic nerves to stressors. Circulation 91 (2), 351–358. https://doi.org/10.1161/01.CIR.91.2.351.

Farr, J.N., Charkoudian, N., Barnes, J.N., et al., 2012. Relationship of sympathetic activity to bone microstructure, turnover, and plasma osteopontin levels in women. J. Clin. Endocrinol. Metab. 97 (11), 4219–4227. https://doi.org/10.1210/jc.2012-2381.

Ferguson, V.L., Ayers, R.A., Bateman, T.A., Simske, S.J., 2003. Bone development and age-related bone loss in male C57BL/6J mice. Bone 33 (3), 387–398. https://doi.org/10.1016/S8756-3282(03)00199-6.

Fu, L., Patel, M.S., Bradley, A., Wagner, E.F., Karsenty, G., 2005. The molecular clock mediates leptin-regulated bone formation. Cell 122 (5), 803–815. https://doi.org/10.1016/j.cell.2005.06.028.

Fukumoto, S., Martin, T.J., 2009. Bone as an endocrine organ. Trends Endocrinol. Metab. 20 (5), 230–236. https://doi.org/10.1016/J.TEM.2009.02.001.

Galli, A., DeFelice, L.J., Duke, B.J., Moore, K.R., Blakely, R.D., 1995. Sodium-dependent norepinephrine-induced currents in norepinephrine-transporter-transfected HEK-293 cells blocked by cocaine and antidepressants. J. Exp. Biol. 198 (Pt 10), 2197–2212.

Graham, S., Hammond-Jones, D., Gamie, Z., Polyzois, I., Tsiridis, E., Tsiridis, E., 2008. The effect of β-blockers on bone metabolism as potential drugs under investigation for osteoporosis and fracture healing. Expert Opin. Investig. Drugs 17 (9), 1281–1299. https://doi.org/10.1517/13543784.17.9.1281.

Greenbaum, A., Chan, K.Y., Dobreva, T., et al., 2017. Bone CLARITY: clearing, imaging, and computational analysis of osteoprogenitors within intact bone marrow. Sci. Transl. Med. 9 (387).

Haenisch, B., Bilkei-Gorzo, A., Caron, M.G., Bönisch, H., 2009. Knockout of the norepinephrine transporter and pharmacologically diverse antidepressants prevent behavioral and brain neurotrophin alterations in two chronic stress models of depression. J. Neurochem. 111 (2), 403–416. https://doi.org/10.1111/j.1471-4159.2009.06345.x.

Hart, E.C.J., Charkoudian, N., 2014. Sympathetic neural regulation of blood pressure: influences of sex and aging. Physiology (Bethesda) 29 (1), 8–15. https://doi.org/10.1152/physiol.00031.2013.

Iwase, S., Mano, T., Watanabe, T., Saito, M., Kobayashi, F., 1991. Age-related changes of sympathetic outflow to muscles in humans. J. Gerontol. 46 (1), M1–M5.

Kajimura, D., Hinoi, E., Ferron, M., et al., 2011. Genetic determination of the cellular basis of the sympathetic regulation of bone mass accrual. J. Exp. Med. 208 (4), 841–851. https://doi.org/10.1084/jem.20102608.

Kajimura, D., Paone, R., Mann, J.J., Karsenty, G., 2014. Foxo1 regulates Dbh expression and the activity of the sympathetic nervous system in vivo. Mol. Metab. 3 (7), 770–777. https://doi.org/10.1016/j.molmet.2014.07.006.

Karsenty, G., Oury, F., 2014. Regulation of male fertility by the bone-derived hormone osteocalcin. Mol. Cell. Endocrinol. 382 (1), 521–526. https://doi.org/10.1016/j.mce.2013.10.008.

Katayama, Y., Battista, M., Kao, W.-M., et al., 2006. Signals from the sympathetic nervous system regulate hematopoietic stem cell egress from bone marrow. Cell 124 (2), 407–421. https://doi.org/10.1016/j.cell.2005.10.041.

Khrimian, L., Obri, A., Ramos-Brossier, M., et al., 2017. Gpr158 mediates osteocalcin's regulation of cognition. J. Exp. Med. 214 (10), 2859–2873. https://doi.org/10.1084/jem.20171320.

Ma, Y., Nyman, J.S., Tao, H., Moss, H.H., Yang, X., Elefteriou, F., 2011. β2-adrenergic receptor signaling in osteoblasts contributes to the catabolic effect of glucocorticoids on bone. Endocrinology 152 (4), 1412–1422. https://doi.org/10.1210/en.2010-0881.

Ma, Y., Krueger, J.J., Redmon, S.N., et al., 2013. Extracellular norepinephrine clearance by the norepinephrine transporter is required for skeletal homeostasis. J. Biol. Chem. 288, 30105–30113. https://doi.org/10.1074/jbc.M113.481309.

Mach, D., Rogers, S., Sabino, M., et al., 2002. Origins of skeletal pain: sensory and sympathetic innervation of the mouse femur. Neuroscience 113 (1), 155–166. https://doi.org/10.1016/S0306-4522(02)00165-3.

Madisen, L., Zwingman, T.A., Sunkin, S.M., et al., 2010. A robust and high-throughput Cre reporting and characterization system for the whole mouse brain. Nat. Neurosci. 13 (1), 133–140. https://doi.org/10.1038/nn.2467.

Mai, T.H., Wu, J., Diedrich, A., Garland, E.M., Robertson, D., 2014. Calcitonin gene-related peptide (CGRP) in autonomic cardiovascular regulation and vascular structure. J. Am. Soc. Hypertens. 8 (5), 286–296. https://doi.org/10.1016/j.jash.2014.03.001.

Mandela, P., Ordway, G.A., 2006. The norepinephrine transporter and its regulation. J. Neurochem. 97 (2), 310–333. https://doi.org/10.1111/j.1471-4159.2006.03717.x.

Méndez-Ferrer, S., Michurina, T.V., Ferraro, F., et al., 2010. Mesenchymal and haematopoietic stem cells form a unique bone marrow niche. Nature 466 (7308), 829–834. https://doi.org/10.1038/nature09262.

Oury, F., Ferron, M., Huizhen, W., et al., 2013. Osteocalcin regulates murine and human fertility through a pancreas-bone-testis axis. J. Clin. Invest. 123 (6), 2421–2433. https://doi.org/10.1172/JCI65952.

Paschalis, E.P., Fratzl, P., Gamsjaeger, S., et al., August 2015. Aging vs postmenopausal osteoporosis: bone composition and maturation kinetics at actively forming trabecular surfaces of female subjects aged 1 to 84 years old. J. Bone Miner. Res. https://doi.org/10.1002/jbmr.2696.

Rached, M.-T., Kode, A., Xu, L., et al., 2010. FoxO1 is a positive regulator of bone formation by favoring protein synthesis and resistance to oxidative stress in osteoblasts. Cell Metab. 11 (2), 147–160. https://doi.org/10.1016/J.CMET.2010.01.001.

Rasmussen, L.E., Nedergaard, O.A., 2003. Effects of reboxetine on sympathetic neuroeffector transmission in rabbit carotid artery. J. Pharmacol. Exp. Ther. 306 (3), 995–1002. https://doi.org/10.1124/jpet.103.052233.

Reid, I.R., Gamble, G.D., Grey, A.B., et al., 2005. beta-Blocker use, BMD, and fractures in the study of osteoporotic fractures. J. Bone Miner. Res. 20 (4), 613–618. https://doi.org/10.1359/JBMR.041202.

Rejnmark, L., Vestergaard, P., Kassem, M., et al., 2004. Fracture risk in perimenopausal women treated with beta-blockers. Calcif. Tissue Int. 75 (5), 365–372. https://doi.org/10.1007/s00223-004-0222-x.

Robling, A.G., Niziolek, P.J., Baldridge, L.A., et al., 2008. Mechanical stimulation of bone in vivo reduces osteocyte expression of Sost/sclerostin. J. Biol. Chem. 283 (9), 5866–5875. https://doi.org/10.1074/jbc.M705092200.

Rosen, C.J., 2008. Bone remodeling, energy metabolism, and the molecular clock. Cell Metab. 7 (1), 7–10. https://doi.org/10.1016/j.cmet.2007.12.004.

Rosen, C.J., 2016. Skeletal integration of energy homeostasis: translational implications. Bone 82, 35–41. https://doi.org/10.1016/j.bone.2015.07.026.

Sato, M., Asada, N., Kawano, Y., et al., 2013. Osteocytes regulate primary lymphoid organs and fat metabolism. Cell Metab. 18 (5), 749–758. https://doi.org/10.1016/j.cmet.2013.09.014.

Schömig, E., Fischer, P., Schönfeld, C.L., Trendelenburg, U., 1989. The extent of neuronal re-uptake of 3H-noradrenaline in isolated vasa deferentia and atria of the rat. Naunyn Schmiedeberg's Arch. Pharmacol. 340 (5), 502–508.

Shen, H., Grimston, S., Civitelli, R., Thomopoulos, S., 2015. Deletion of connexin43 in osteoblasts/osteocytes leads to impaired muscle formation in mice. J. Bone Miner. Res. 30 (4), 596–605. https://doi.org/10.1002/jbmr.2389.

Song, H.J., Lee, J., Kim, Y.-J., et al., 2012. β1 selectivity of β-blockers and reduced risk of fractures in elderly hypertension patients. Bone 51 (6), 1008–1015. https://doi.org/10.1016/j.bone.2012.08.126.

Takeda, S., Elefteriou, F., Levasseur, R., et al., 2002. Leptin regulates bone formation via the sympathetic nervous system. Cell 111 (3), 305–317.

Tiede-Lewis, L.M., Xie, Y., Hulbert, M.A., et al., 2017. Degeneration of the osteocyte network in the C57BL/6 mouse model of aging. Aging (Albany NY) 9 (10), 2190–2208. https://doi.org/10.18632/aging.101308.

Toulis, K.A., Hemming, K., Stergianos, S., Nirantharakumar, K., Bilezikian, J.P., 2014. β-Adrenergic receptor antagonists and fracture risk: a meta-analysis of selectivity, gender, and site-specific effects. Osteoporos. Int. 25 (1), 121–129. https://doi.org/10.1007/s00198-013-2498-z.

Turker, S., Karatosun, V., Gunal, I., 2006. Beta-blockers increase bone mineral density. Clin. Orthop. Relat. Res. 443, 73–74. https://doi.org/10.1097/01.blo.0000200242.52802.6d.

Veldhuis-Vlug, a G., El Mahdiui, M., Endert, E., Heijboer, a C., Fliers, E., Bisschop, P.H., 2012. Bone resorption is increased in Pheochromocytoma patients and normalizes following adrenalectomy. J. Clin. Endocrinol. Metab. 97, E2093–E2097. https://doi.org/10.1210/jc.2012-2823.

Vincent, S., Bieck, P.R., Garland, E.M., et al., 2004. Clinical assessment of norepinephrine transporter blockade through biochemical and pharmacological profiles. Circulation 109 (25), 3202–3207. https://doi.org/10.1161/01.CIR.0000130847.18666.39.

Wei, J., Shimazu, J., Makinistoglu, M.P., et al., 2015. Glucose uptake and Runx2 synergize to orchestrate osteoblast differentiation and bone formation. Cell 161 (7), 1576–1591. https://doi.org/10.1016/j.cell.2015.05.029.

Wiens, M., Etminan, M., Gill, S.S., Takkouche, B., 2006. Effects of antihypertensive drug treatments on fracture outcomes: a meta-analysis of observational studies. J. Intern. Med. 260 (4), 350–362. https://doi.org/10.1111/j.1365-2796.2006.01695.x.

Wong, E.H.F., Sonders, M.S., Amara, S.G., et al., 2000. Reboxetine: a pharmacologically potent, selective, and specific norepinephrine reuptake inhibitor. Biol. Psychiatry 47 (9), 818–829. https://doi.org/10.1016/S0006-3223(99)00291-7.

Xiong, J., Onal, M., Jilka, R.L., Weinstein, R.S., Manolagas, S.C., O'Brien, C.A., 2011. Matrix-embedded cells control osteoclast formation. Nat. Med. 17 (10), 1235–1241. https://doi.org/10.1038/nm.2448.

Xu, H., Gu, S., Riquelme, M.A., et al., 2015. Connexin 43 channels are essential for Normal bone structure and osteocyte viability. J. Bone Miner. Res. 30 (3), 436–448. https://doi.org/10.1002/jbmr.2374.

Yamashita, A., Nishikawa, S., Rancourt, D.E., 2010. Microenvironment modulates osteogenic cell lineage commitment in differentiated embryonic stem cells. Aziz SA, ed. PLoS One 5 (3), e9663. https://doi.org/10.1371/journal.pone.0009663.

Yamazaki, K., Allen, T.D., 1990. Ultrastructural morphometric study of efferent nerve terminals on murine bone marrow stromal cells, and the recognition of a novel anatomical unit: the neuro-reticular complex? Am. J. Anat. 187 (3), 261–276. https://doi.org/10.1002/aja.1001870306.

Yang, S., Nguyen, N.D., Center, J.R., Eisman, J.A., Nguyen, T.V., 2011. Association between beta-blocker use and fracture risk: the dubbo osteoporosis epidemiology study. Bone 48 (3), 451–455. https://doi.org/10.1016/j.bone.2010.10.170.

Yang, S., Nguyen, N.D., Eisman, J.A., Nguyen, T.V., 2012. Association between beta-blockers and fracture risk: a Bayesian meta-analysis. Bone 51 (5), 969–974. https://doi.org/10.1016/j.bone.2012.07.013.

Yang, B., Treweek, J.B., Kulkarni, R.P., et al., 2014. Single-cell phenotyping within transparent intact tissue through whole-body clearing. Cell 158 (4), 945–958. https://doi.org/10.1016/j.cell.2014.07.017.

Yirmiya, R., Goshen, I., Bajayo, A., et al., 2006. Depression induces bone loss through stimulation of the sympathetic nervous system. Proc. Natl. Acad. Sci. U. S. A. 103 (45), 16876–16881. https://doi.org/10.1073/pnas.0604234103.

Zeng, W., Pirzgalska, R.M., Pereira, M.M.A., et al., 2015. Sympathetic neuro-adipose connections mediate leptin-driven lipolysis. Cell 163 (1), 84–94. https://doi.org/10.1016/j.cell.2015.08.055.

Zhou, S., Greenberger, J.S., Epperly, M.W., et al., 2008. Age-related intrinsic changes in human bone-marrow-derived mesenchymal stem cells and their differentiation to osteoblasts. Aging Cell 7 (3), 335–343. https://doi.org/10.1111/j.1474-9726.2008.00377.x.